Electronic Supplementary Material (ESI) for Energy & Environmental Science.
This journal is © The Royal Society of Chemistry 2018

Supplementary Information

Aqueous vs Nonaqueous Zn-Ion Batteries: Consequences of the Desolvation Penalty at the Interface

Dipan Kundu,[a†] Shahrzad Hosseini Vajargah,[a] Liwen Wan,[b,c] Brian Adams,[a,c] David Prendergast[b,c] and Linda F. Nazar[a,c*]

[a] *Department of Chemistry, Waterloo Institute for Nanotechnology, University of Waterloo, 200 University Ave W, Waterloo, Ontario N2L 3G1, Canada*

[b] *The Molecular Foundry, Lawrence Berkeley National Laboratory, Berkeley, CA 94720, USA*

[c] *Joint Center for Energy Storage Research (JCESR), USA*

[†] *Current address: ETH Zürich, Laboratory for Multifunctional Materials, HCI F 503, Vladimir-Prelog-Weg 1-5/10, 8093 Zürich Switzerland*

Table S1. Refined Lattice Parameters for Synthesized $V_3O_7.H_2O$

Diffractometer:	Bruker D8 advance
Radiation	Cu Kα
2θ range	5-80
Step size	0.0085
Sec/step	4
Background	Chebyshev Polynomial
Chemical formula	$V_3O_7.H_2O$
Space group	*Pnam*
a (Å)	16.8714(6)
b (Å)	9.3325(4)
c (Å)	3.6348(1)
α (°)	90
β (°)	90
γ (°)	90
Cell Volume (Å^3)	572.31(3)
R_{exp}	0.967
R_p [%]	1.642
R_{wp} [%]	2.468
χ^2	6.51

*Determined by Rietveld refinement of the XRD data

Table S2. XPS binding energy values for Zn 2p and V 2p components

Sample	Species	Peak positions for Zn/V2p3/2 Zn/V2p1/2 (eV)	Species Percentage (%)	Species	Peak positions for Zn/V2p3/2 Zn/V2p1/2 (eV)	Species Percentage (%)
Pristine cathode	Zn^{2+} - I	-	0	Zn^{2+} - I	-	0
	Zn^{2+} - II	-	0	Zn^{2+} - II	-	0
	V^{5+}	517.42 524.72	75.93	V^{5+}	517.42 524.72	75.93
	V^{4+}	515.90 523.18	24.06	V^{4+}	515.90 523.18	24.06
	V^{3+}	-	0	V^{3+}	- -	0
Discharged cathode	Zn^{2+} - I	1022.33 1045.37	53.81	Zn^{2+} - I	1022.41 1045.53	100
	Zn^{2+} - II	1023.94 1047.00	46.18	Zn^{2+} - II	- -	0
	V^{5+}	519.04 526.26	34.78	V^{5+}	517.31 526.96	66.73
	V^{4+}	517.38 524.74	44.08	V^{4+}	516.64 523.57	33.27
	V^{3+}	515.91 523.36	21.14	V^{3+}	515.91 523.36	0
Charged cathode	Zn^{2+} - I	1022.29 1045.37	100	Zn^{2+} - I	1022.37 1045.43	100
	Zn^{2+} - II	-	0	Zn^{2+} - II	-	0
	V^{5+}	517.72 525.06	70.15	V^{5+}	517.71 525.15	73.24
	V^{4+}	516.33 523.71	29.85	V^{4+}	516.31 523.61	26.76
	V^{3+}	-	0	V^{3+}	-	0

Details of the XPS fits and analyses. XPS analysis was performed on a Thermo ESCALAB 250 instrument configured with a monochromatic Al Kα (1486.6 eV). Spectra were analyzed using CasaXPS software. For the background, a Shirley (vanadium and oxygen) or a Tougaard type function was used. A combination of Gaussian (Y%)-Lorentzian (X%) peak shape functions, defined as GL(X) in CasaXPS was used to fit each component. The suitable mixture of Gaussian-Lorentzian components depends on the natural line-width of the specific core hole and also on the instrument and resolution settings used. In our analysis, for Zn 2p and O 1s spectra, GL(30) was used, whereas for the V 2p region, the best fit was obtained with GL(90), in accordance with the literature.[1] The binding energy values were all calibrated using the adventitious C 1s peak at 284.8 eV. For the fitting of the 2p (V and Zn) component pairs, a peak area ratio of 2:1 for 2p3/2: 2p1/2 was used with 2p1/2 having the higher value of FWHM (full width at half maximum).

While the Zn 2p region provides clear evidence of reversible Zn^{2+} (de)intercalation, the V 2p region demonstrates reversibility of the accompanying vanadium redox behavior, in both aqueous and nonaqueous systems. In the V 2p region, the appearance and the increase in intensity of the lower binding energy components (V^{3+} and V^{4+}) upon discharge characterize the reduction of vanadium in $Zn_xV_3O_7$•H_2O. While the V^{4+} signal intensifies strongly upon discharge in both aqueous and nonaqueous systems, a V^{3+} component also appears in the former, in accord with the reduction to an average valence of $V^{3.33+}$ based on ~ 2 Zn^{2+} intercalation. This is fully reversed upon charge, where the pristine V 2p spectrum is regenerated. Interestingly, for the aqueous system, the discharged V^{5+} signal shifts to a higher binding energy relative to the pristine or the charged V^{5+} component (V $2p_{3/2}$: 519 eV), even though the V^{3+} and V^{4+} signals appear at their expected binding energies. Such a blue shift may correspond to the intercalation of the Zn^{2+} ions and the consequent bonding rearrangements at the remaining V^{5+} sites, the exact nature of which remains unclear. No such shift is observed in the nonaqueous system, which could be due to a smaller degree of Zn^{2+} intercalation.

List of Supporting Figures and Figure Captions

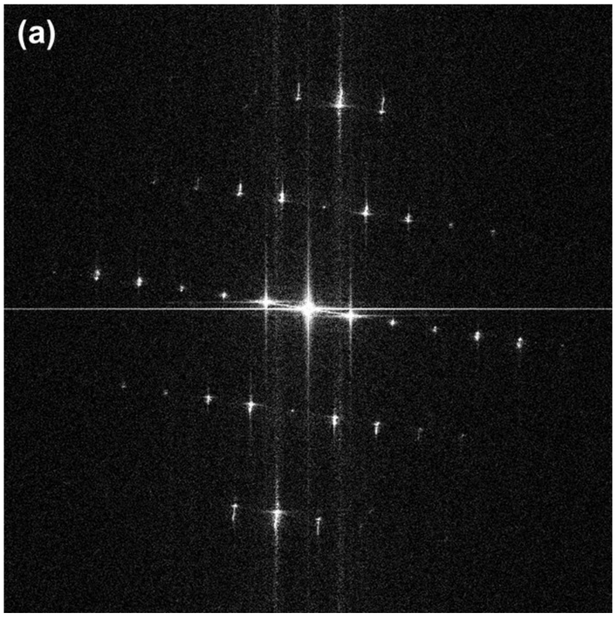

Fig. S1. Fast fourier transform (FFT) of the image in Fig. 1e confirming the single crystalline nature of the $V_3O_7 \bullet H_2O$ nanofibers.

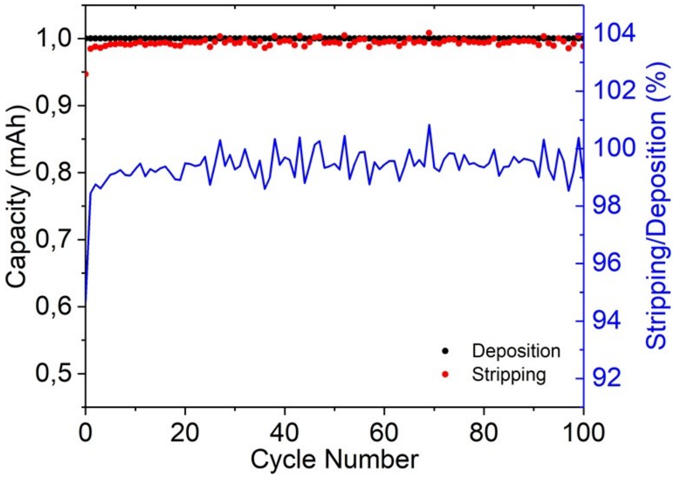

Fig. S2. Galvanostatic zinc plating stripping result obtained using a three-electrode cell with Ti as the working electrode and Zn as the reference and the counter electrode. A current of 1 mA cm^{-2} was applied, limiting the deposition time to 1 h, while a cut off potential of 0.7 V (vs. Zn^{2+}/Zn reference) was used for the stripping process. Except for the initial cycles, nearly 99.5% Coulombic efficiency is observed.

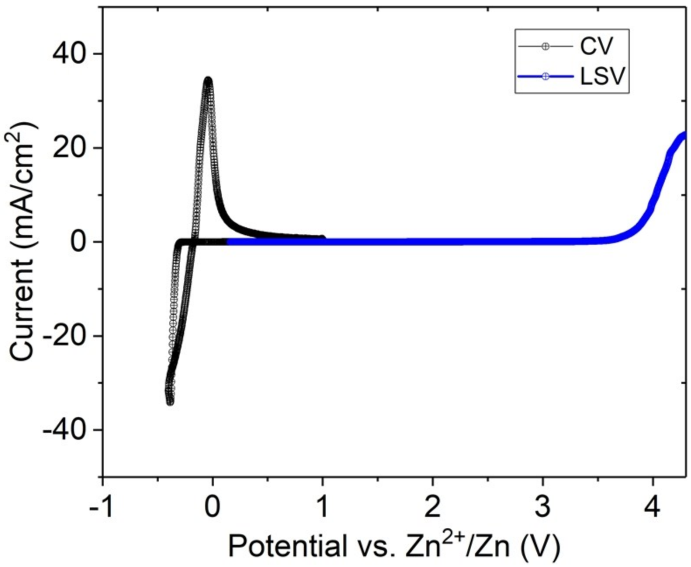

Fig. S3. Cyclic voltammogram (CV) and linear sweep voltammogram (LSV) for the 0.25 M ZnOTf/AN electrolyte showing reversible Zn plating stripping in the nonaqueous electrolyte and the corresponding upper limit of the voltage window (~3.6 V). The experiment was performed in a three-electrode cell using Ti rod as the working electrode and Zn as the counter and reference electrode at a scan rate of 5 mV/sec.

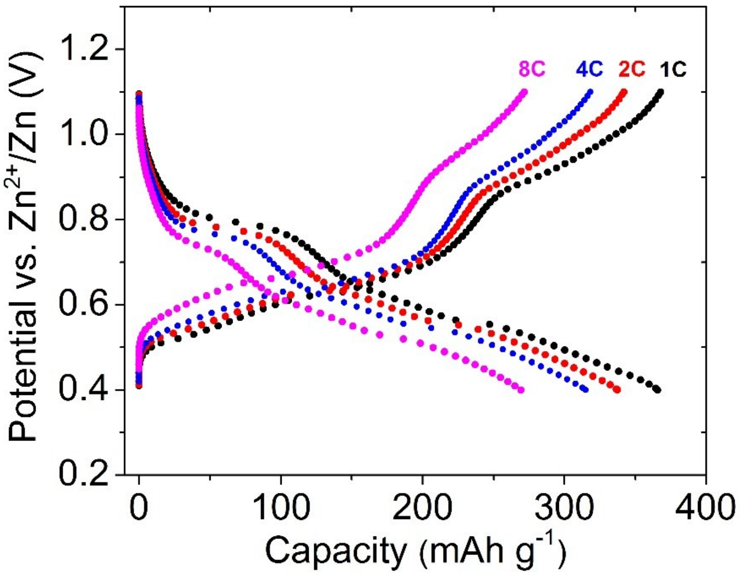

Fig. S4. Galvanostatic discharge and charge profiles of the $V_3O_7.H_2O$ freestanding cathode at different current densities in 1 M $ZnSO_4$-H_2O electrolyte. Here, 1C corresponds to a current rate of 375 mA g^{-1} and rest of the current rates are defined w.r.t. it. The discharge-charge cycle (1st charge and 2nd discharge profiles) shown here is the first reversible cycle.

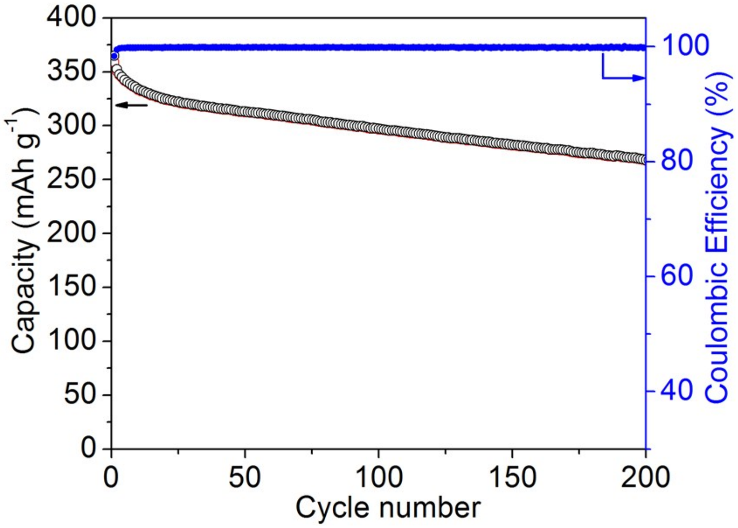

Fig. S5. Cycling performance and the corresponding Coulombic efficiency at a 1C (375 mA g^{-1}) rate showing ~75 % of the capacity retention after 200 cycles for the aqueous system.

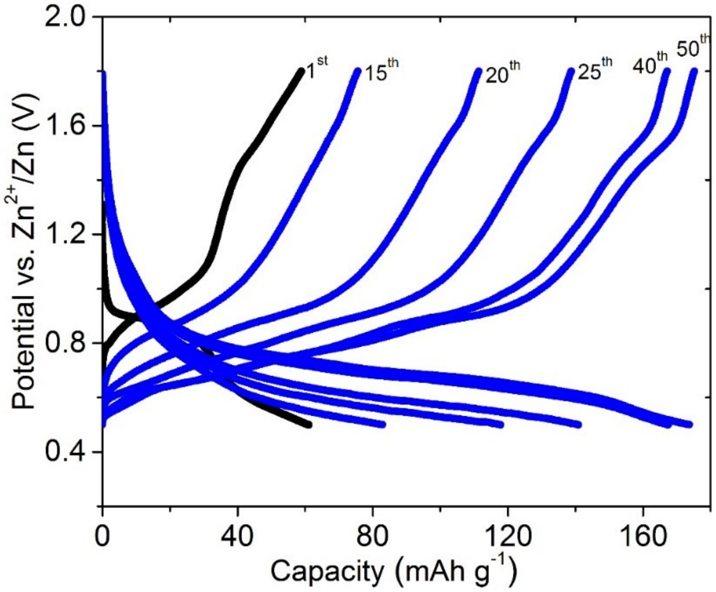

Fig. S6. Galvanostatic discharge-charge profiles of the $V_3O_7.H_2O$ freestanding cathode at a current density of 5 mA g^{-1} in 0.25 M $Zn(CF_3SO_3)_2$-acetonitrile electrolyte. The capacity value increases with cycling accompanied by a little modification to the voltage profiles before the steadying around 175 mAh g^{-1} after 50 cycles.

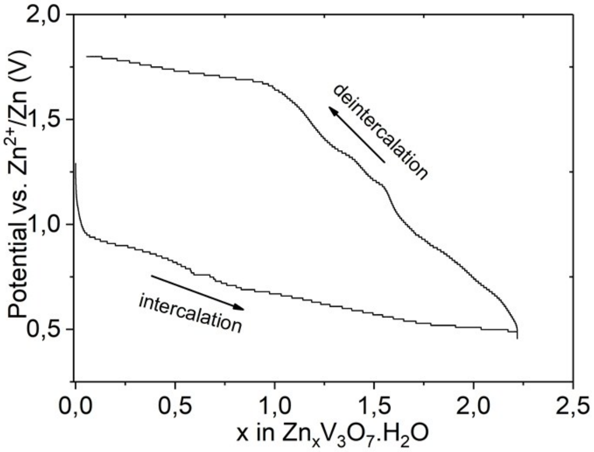

Fig. S7. Potential as a function of zinc concentration in $V_3O_7.H_2O$ obtained by a controlled potential Coulometry in 0.25 M $Zn(CF_3SO_3)_2$-acetonitrile electrolyte in 0.5 – 1.8 V window. In this method, the potential of the working electrode ($V_3O_7.H_2O$ cathode) was changed in steps of 10 mV and held at constant potentials until the current dropped below 0.25 μA in each step.

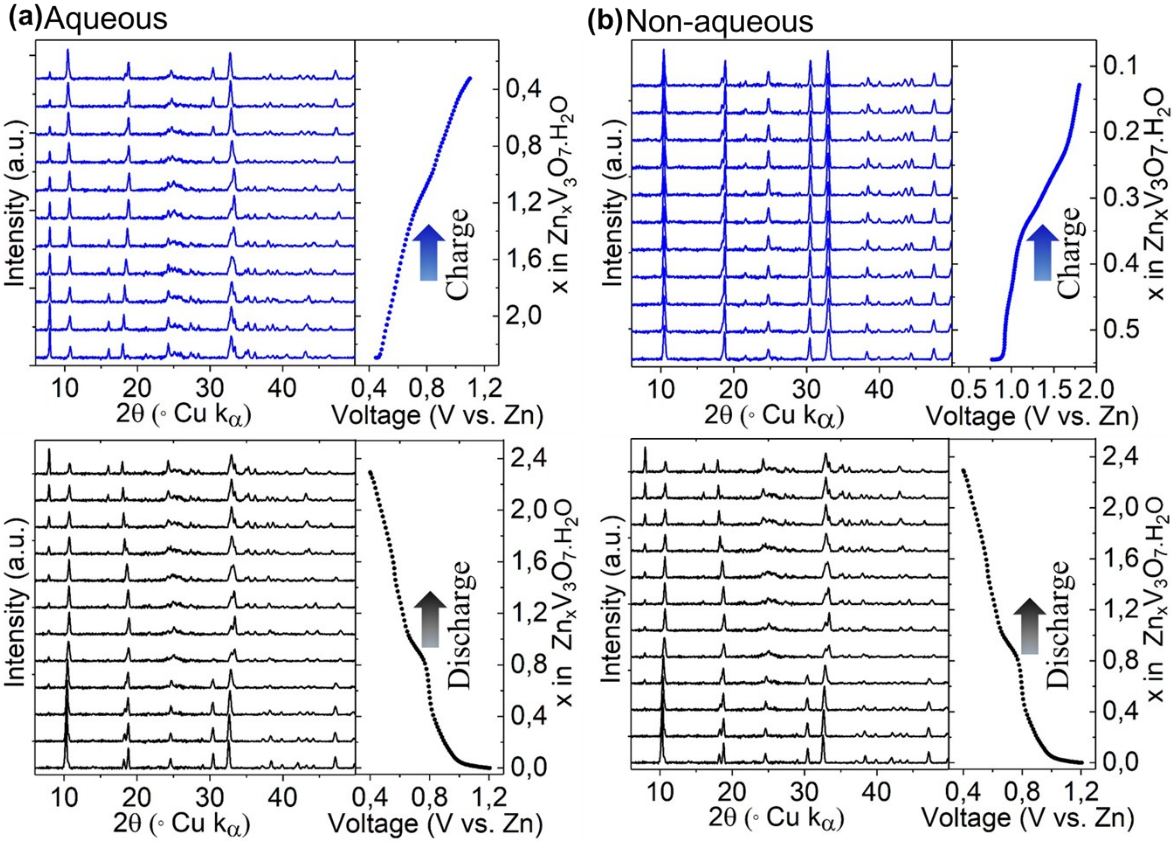

Fig. S8. Operando X-ray diffraction study of the $V_3O_7.H_2O$ electrode during cycling in the aqueous (a) and in the nonaqueous (b) electrolytes. Both show the evolution of the XRD pattern as a function of Zn^{2+} content in $V_3O_7.H_2O$ during the first electrochemical discharge and charge cycles.

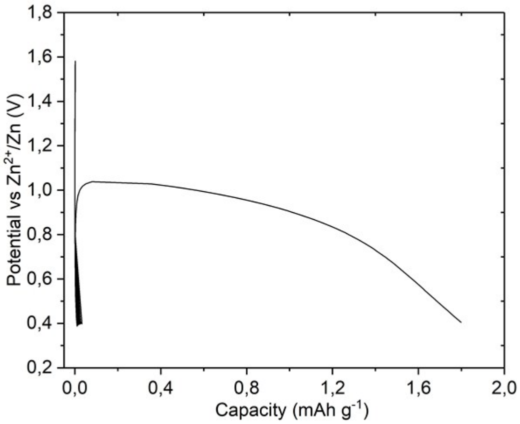

Fig. S9. Galvanostatic discharge/charge cycling of $V_3O_7.H_2O$ in pH 4 H_2SO_4 electrolyte in a three electrode cell with platinum as the counter and zinc as the reference electrode. A current density of 50 mA g^{-1} was applied. Since virtually no capacity was observed after the 1st discharge, the data appear bunched together. The result clearly demonstrates that proton intercalation does not contribute to the electrochemical performance observed in 1 M $ZnSO_4$, H_2O electrolyte, which also has a pH of 4.

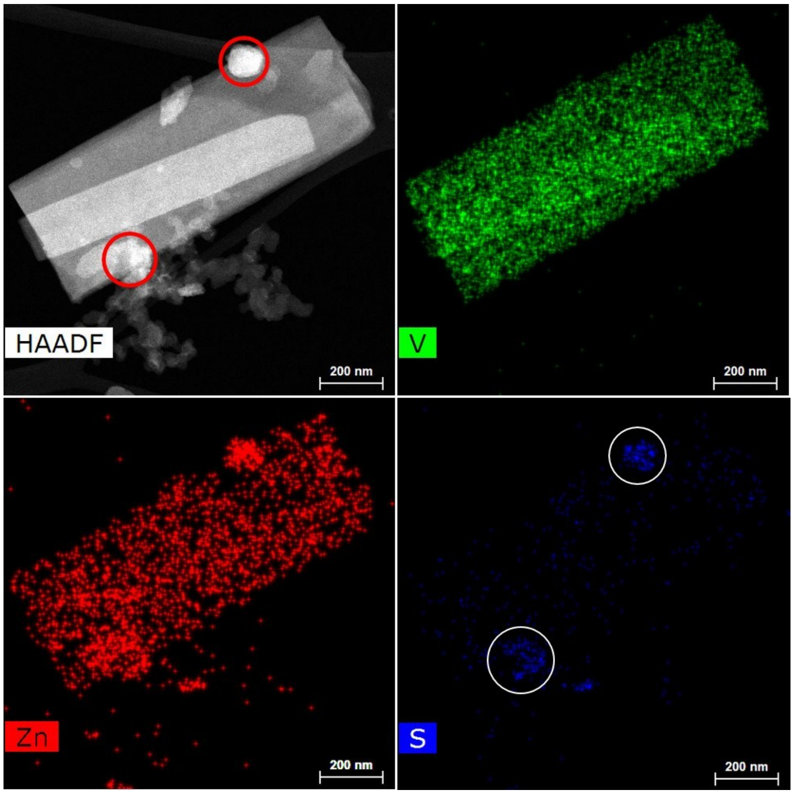

Figure S7. HAADF-STEM image of a discharged (zinc intercalated) $V_3O_7.H_2O$ fiber and the corresponding EDX elemental maps.

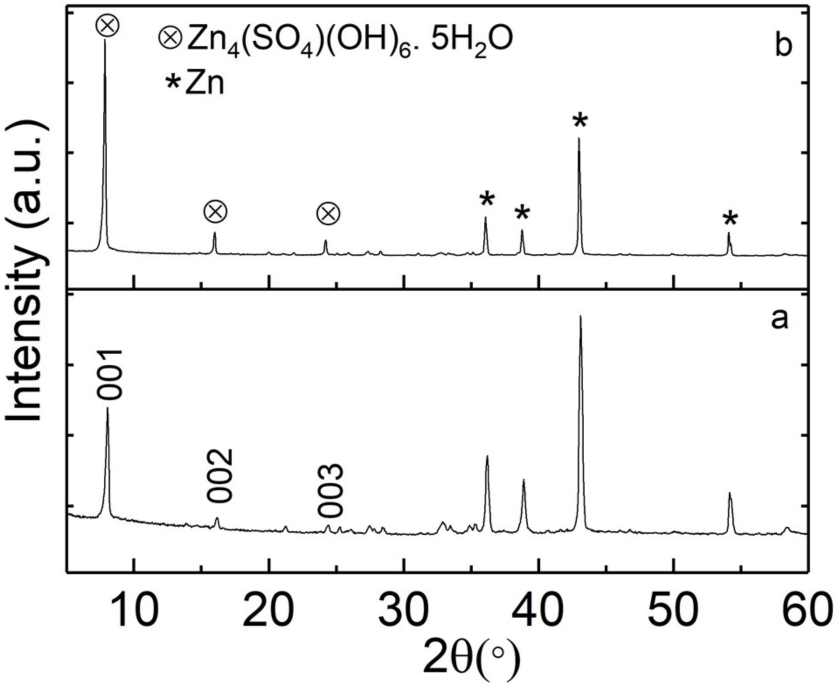

Fig. S8. X-ray diffraction of the Zn electrode of a (a) Zn – $V_3O_7.H_2O$ cell and a (b) Zn – Zn symmetric cell showing strong reflections of $Zn_4(SO_4)(OH)_6.5H_2O$ in addition to the underlying Zn peaks. In (a) the Zn electrode was studied after 5th discharge of the cell; for (b) the Zn deposited electrode was studied after Zn deposition at 1 mA current for 24 h.

Discussion of Figs. S6 – S8: mechanism of $Zn_4(SO_4)(OH)_6.nH_2O$ formation. For α-MnO_2, Pan *et al*. found that H^+ from the aqueous electrolyte electrochemically intercalates into MnO_2 to form MnOOH, and the residual OH^- chemically reacts with Zn^{2+} and SO_4^{2-} resulting in a flaky precipitate of $Zn_4(SO_4)(OH)_6.nH_2O$ (n = 3 or 5).[2] Lee *et al.* proposed a seemingly different mechanism[3] involving disproportionation and dissolution of Mn^{3+} in the electrolyte, which leads to a gradual increase in the pH of the electrolyte finally causing $Zn_4(SO_4)(OH)_6.nH_2O$ particles to precipitate on the electrode surface at around pH 5.5 – 5.7. However, for V_3O_7•H_2O, we neither observed any H^+ intercalation from a pH 4 - H_2SO_4 electrolyte (same pH as 1 M $ZnSO_4$ in H_2O; **Fig. S6**), nor was there any noticeable change in the pH of the electrolyte during cycling, as probed *in situ* by a pH meter. There was only a mild increase pH from an initial value of 4 to 4.2 after 10 cycles. Furthermore, elemental mapping using EDX in STEM revealed a very homogeneous Zn distribution in the fibers corresponding to the intercalated Zn, whereas $Zn_4(SO_4)(OH)_6.nH_2O$ was identified as agglomerated particles (**Fig. S7**) from the sulfur map, forming on and around the vanadate fibers. Notably, $Zn_4(SO_4)(OH)_6.nH_2O$ particles were found to be only sparsely distributed in the discharged electrode. They are highly crystalline lamellae, leading to strong *00l* reflections observed in our *operando* X-ray studies. To our surprise, we also detected strong X-ray reflections of $Zn_4(SO_4)(OH)_6.nH_2O$ (n = 5) on the Zn electrode of both electrochemically cycled Zn - V_3O_7•H_2O *and* Zn - Zn symmetric cells (**Fig. S8**); for the latter, the *001* reflections of this phase (JCPDS #61114) even overwhelmed the reflections from the background Zn metal. This observation leads us to speculate that $Zn_4(SO_4)(OH)_6.nH_2O$ forms by a side reaction involving dissolved O_2 in the electrolyte, Zn^{2+}, SO_4^{2}, and H_2O as follows.

$$\frac{1}{2} O_2 + H_2O + e^- \rightarrow 2OH^- \tag{1}$$

$$4Zn^{2+} + 6OH^- + SO_4^{2-} + nH_2O \rightarrow Zn_4(SO_4)(OH)_6.nH_2O \tag{2}$$

Dissolved oxygen is first reduced to OH^- which then combines with Zn^{2+} and SO_4^{2-} and precipitates.[4] This mechanism has been proposed for zinc hydroxysulfate electrodeposition on a polypyrrole film from 0.1 M $ZnSO_4$ aqueous solution at 0 V against SCE (saturated calomel electrode).[3] This corresponds to 1 V against Zn^{2+}/Zn, which is only slightly higher than the voltage (~ 0.8 V) at which we observe the initiation of $Zn_4(SO_4)(OH)_6.5H_2O$ precipitation (see Fig. 3, main text).

The mechanism of hydroxysulfate disappearance during electrochemical charge process observed during the *operando* X-ray studies is not as clear. Its chemical conversion to ZnO and vice versa as a function of changing SO_4^{2-} ion concentration[5] (see equation 3) during the subsequent charge-discharge is a feasible reaction path, but further studies are required to confirm such a process.

$$Zn_4(SO_4)(OH)_6.5H_2O \leftrightarrow Zn^{2+} + 3ZnO + SO_4^{2-} + 5H_2O \tag{3}$$

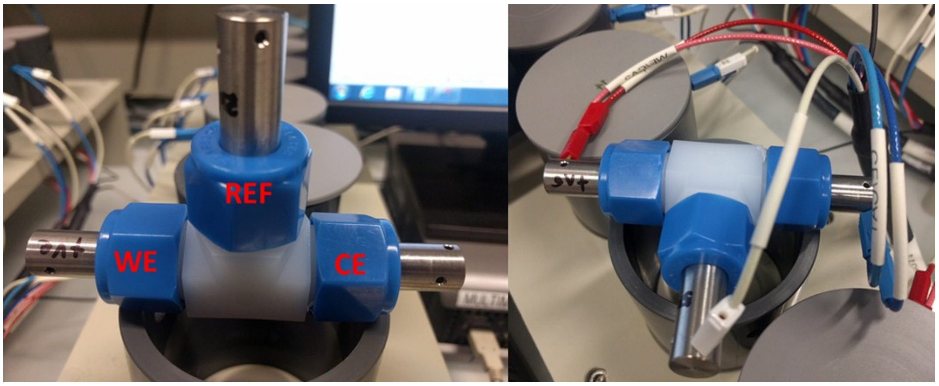

Fig. S12. T-shaped three-electrode cell used for the impedance study

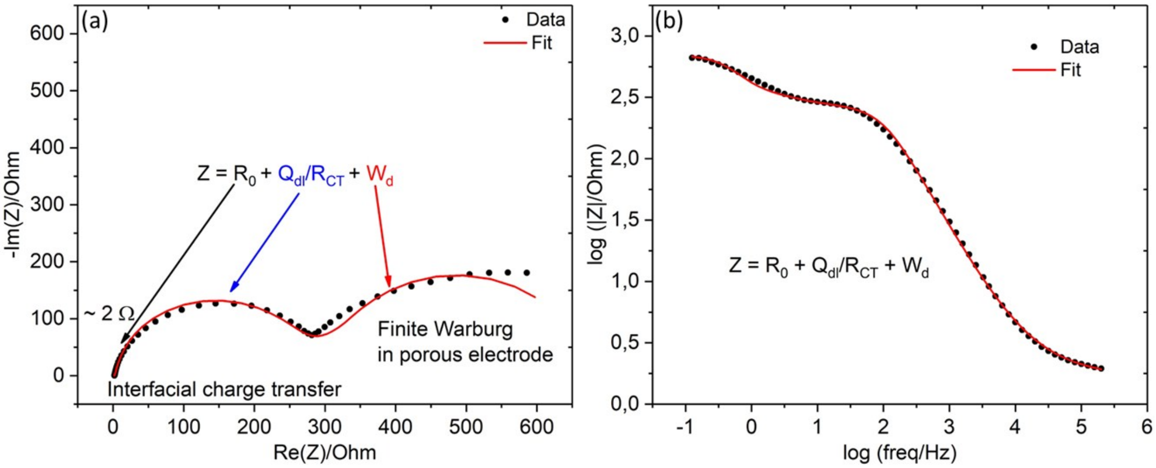

Fig. S13. (a) Nyquist and (b) Bode impedance plot (black markers) for the $V_3O_7.H_2O$ working electrode in the 0.25 M $Zn(CF_3SO_3)_2$-acetonitrile electrolyte and the corresponding fit (red line) to the model $Z = R_0 + Q_{dl}/R_{CT} + W_d$, where Z is the overall impedance, R_0 is the Ohmic resistance, Q_{dl} stands for double layer capacitance (or geometric capacitance), R_{CT} represents the resistance to the charge transfer at the electrode/electrolyte interface, and W_d defines the finite (bounded) Warburg element for diffusion of ions in the porous electrode network. The values obtained from the fit are: $R_0 = 1.6\ \Omega$, $Q_{dl} = Q1 = 6.842*10^{-6}\ F.s^n$ ($n = 0.92$), $R_{CT} = 302\ \Omega$, and $R_d = 460\ \Omega$ ($\tau_d = 0.855$ s) for the bounded Warburg element.

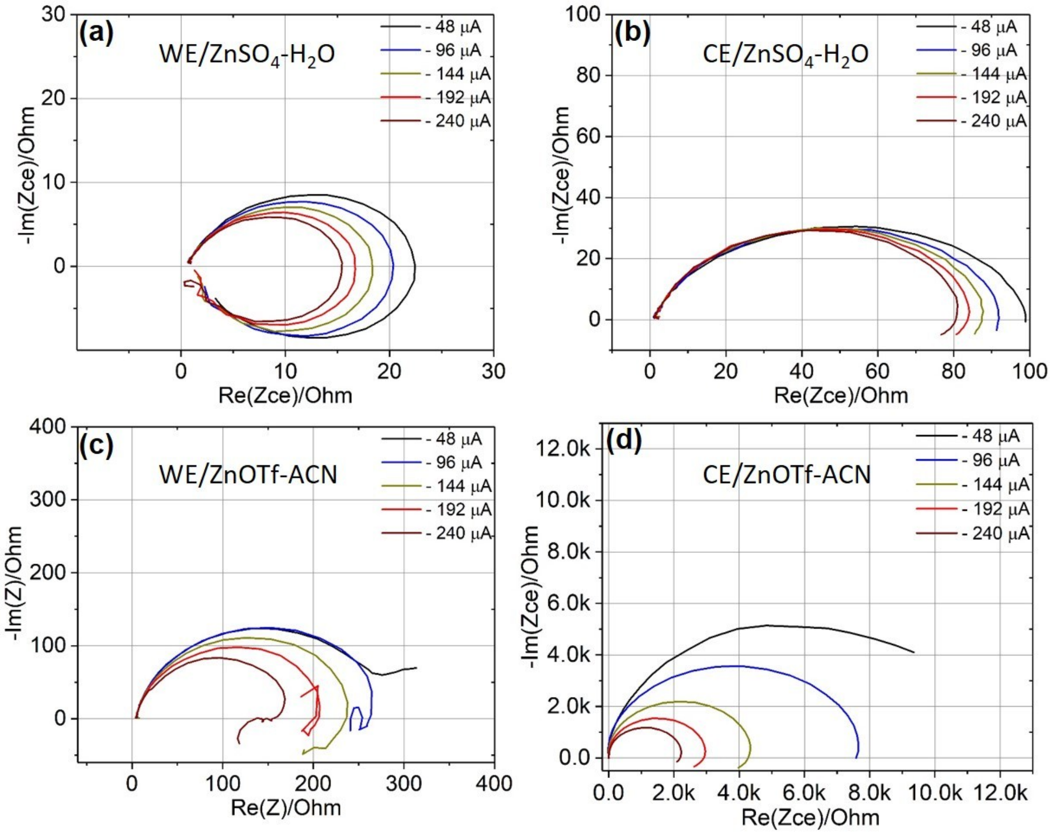

Fig. S14. Complex plane impedance plots for $V_3O_7.H_2O$ working electrodes (WE) and Zn counter electrodes (CE) in the aqueous and non-aqueous electrolytes as labelled. Top row: (a) $V_3O_7.H_2O$ WE in 1 M $ZnSO_4$-H_2O; (b) Zn CE in in 1 M $ZnSO_4$-H_2O. Bottom row: c) $V_3O_7.H_2O$ WE in 0.25 M $Zn(CF_3SO_3)_2$-acetonitrile; d) Zn CE in 0.25 M $Zn(CF_3SO_3)_2$-acetonitrile. EIS measurements were carried out by applying a galvanostatic signal of 50 µA at OCV under five different negative dc current bias (see figure inset) at room temperature (~25˚C). A frequency range of 200 kHz – 1 Hz was used for all the measurements. The dc bias was applied continuously during each impedance measurement and the bias was increased in steps. A minor difference in the low frequency (right side) plots is apparent here relative to those shown in Figure 6 (manuscript), which is due to a higher low-frequency cut off 1 Hz compared to 0.01 Hz for the data in Figure 6, and a different instrument being used to collect the data plotted here. Clearly, increase of the dc bias current results in the shrinking of the semicircles (decrease of R_{CT}) observed for both the electrodes in both systems, although the semicircles mostly retain their shape in the medium frequency range. This observation unambiguously proves that the semicircle we observe in the high-medium frequency region corresponds to the charge transfer process at the electrode/electrolyte interface. We note that charge transfer can be broken down into two steps: desolvation/adsorption of the charged intermediate at the electrode surface followed by an electron transfer step. The latter process is further driven by increasing the dc bias current, and is manifested by the observed decrease in the inductance loop (positive quadrant arc).

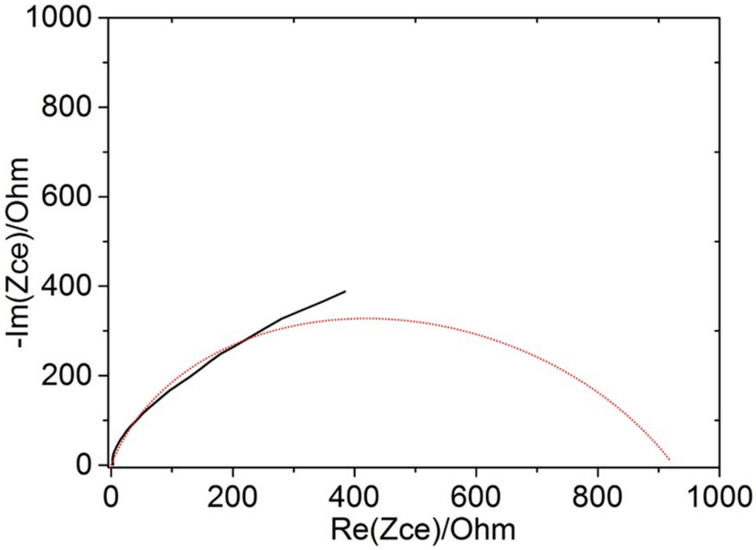

Fig. S15. Complex plane impedance plot of the zinc counter (CE) electrode in the nonaqueous system (black line) after 50 discharge-charge cycles. The red arc here extrapolates the corresponding charge transfer resistance value (R_{CT}) at the Zn electrode, clearly showing a drop in the R_{CT} (refer to Fig. 6b, manuscript) upon repeated zinc stripping and deposition.

References

1 M. C. Biesinger, L. W. M. Lau, A. R. Gersonb and R. S. C. Smart, *Appl. Surf. Sci*., 2010, **257**, 887-898.

2 H. Pan, Y. Shao, P. Yan, Y. Cheng, K. S. Han, Z. Nie, C. Wang, J. Yang, X. Li, X., P. Bhattacharya, K. T. Mueller and J. Liu, *Nat. Energy*, 2016, **1**, 16039.

3 B. Lee, H. R. Lee, H. Kim, K. Y. Chung, B. W. Cho and S. H. Oh, *Chem. Commun.*, 2015, **51**, 9265-9268.

4 E. Andreoli, D. A. Rooney, W. Redington, R. Gunning, and C. B. Breslin, *J. Nanosci. Nanotechnol*. 2012, **12**, 338-349

5 Y. Liu and Z Yang, *RSC Adv*. 2016, **6**, 68584-68591.